GFZ

Helmholtz-Zentrum
POTSDAM

Insights Into Complex Subdecimeter Fracturing Processes Occurring During a Water Injection Experiment at Depth in Äspö Hard Rock Laboratory, Sweden

G. Kwiatek[1,2] iD, P. Martínez-Garzón[1] iD, K. Plenkers[3], M. Leonhardt[1], A. Zang[1,4], S. von Specht[1], G. Dresen[1,4], and M. Bohnhoff[1,2] iD

[1]Helmholtz Centre Potsdam, GFZ German Research Centre for Geosciences, Potsdam, Germany, [2]Free University Berlin, Berlin, Germany, [3]GMuG Gesellschaft für Materialprüfung und Geophysik mbH, Bad Nauheim, Germany, [4]University of Potsdam, Potsdam, Germany

Abstract We investigate the source characteristics of picoseismicity ($M_w < -2$) recorded during a hydraulic fracturing in situ experiment performed in the underground Äspö Hard Rock Laboratory, Sweden. The experiment consisted of six stimulations driven by three different water injection schemes and was performed inside a 28-m-long, horizontal borehole located at 410-m depth. The fracturing processes were monitored with a variety of seismic networks including broadband seismometers, geophones, high-frequency accelerometers, and acoustic emission sensors thereby covering a wide frequency band between 0.01 and 100,000 Hz. Here we study the high-frequency signals with dominant frequencies exceeding 1000 Hz. The combined seismic network allowed for detection and detailed analysis of 196 small-scale seismic events with moment magnitudes $M_W < -3.5$ (source sizes of decimeter scale) that occurred solely during the stimulations and shortly after. The double-difference relocated hypocenter catalog as well as source parameters were used to study the physical characteristics of the induced seismicity and then compared to the stimulation parameters. We observe a spatiotemporal migration of the picoseismic events away and toward the injection intervals in direct correlation with changes in the hydraulic energy (product of fluid injection pressure and injection rate). We find that the total radiated seismic energy is extremely low with respect to the product of injected fluid volume and pressure (hydraulic energy). The radiated seismic energy correlates well with the hydraulic energy rate. The obtained fault plane solutions for particularly well-characterized events signify the reactivation of preexisting rock defects under influence of increased pore fluid pressure on fault plane orientations in good correspondence with the local stress field orientation.

1. Introduction

Understanding the relation between reservoir engineering operations and corresponding seismic response is important toward optimization of hydrocarbon production and mitigating anthropogenic seismic hazard. McGarr (2014) suggested that the maximum magnitude of induced seismicity may have an upper limit related to the total amount of fluid injected into the rock formation following $M_{max} = G\Delta V$, where G is the shear modulus and ΔV is the fluid volume injected into the reservoir. However, for hydraulic fracturing operations (Galis et al., 2017; Goodfellow et al., 2015; Maxwell, 2013) and some reservoir treatments in geothermal systems (Kwiatek et al., 2015; Zang et al., 2014), the observed maximum magnitude is significantly lower than the upper bound from McGarr's empirical relation. The stored energy supplied by hydraulic stimulation $P * \Delta V$ is dissipated in a range of deformation processes (Goodfellow et al., 2015; Halló et al., 2014) such as formation and frictional sliding of new and preexisting fractures that may result in elastic wave propagation (radiated energy) or occur aseismically (Cornet, 2016). These slow deformation processes are evidenced by strainmeter or tiltmeter data (e.g., Guglielmi et al., 2015; Warpinski, 2014). A significant range of seismic injection efficiencies from 10^{-7}% to 10% (the ratio of energy radiated through seismic waves in relation to the hydraulic energy supplied to the reservoir) is reported from a number of hydraulic fracturing operations (e.g., Goodfellow et al., 2015; Maxwell, 2013; Yoon et al., 2015; Zang et al., 2013). It is conceivable that the reduction of the total pumped volume (reduced static strain) or slow injection operations (reduced hydraulic energy rates) may reduce seismic hazard, as originally conceived in Raleigh et al. (1976). However, how the injection volume, flow rate, and injection pressures relate to seismic energy release, and in particular to the occurrence of larger

seismic events, is still a matter of debate (Maxwell et al., 2015; Warpinski, 2013; Warpinski et al., 2012). As of today, there is no approved strategy on how to mitigate induced seismicity, and current approaches mostly focus on reactive traffic light systems reducing flow rates in case of increasing event magnitudes (Bommer et al., 2006; Maxwell, 2013) or modified hydraulic fracturing concepts (Meier et al., 2015; Zang et al., 2013).

Seismic waveform data from hydraulic fracture operations allows analyzing source characteristics and micromechanisms of the processes governing hydraulic fracture nucleation and growth in relation to fluid injection operations. Spatial and temporal characteristics of the seismic catalog typically reveal a complex fracture network generated during hydraulic stimulation (Chitrala et al., 2011; Warpinski, 2014). The radiated energy E_0 released in elastic waves is estimated directly from the waveforms and may provide an estimate of the moment magnitude. Seismic injection efficiency is the ratio between the energy radiated in elastic waves E_0 and total hydraulic energy E_I. It provides an estimate of the deformation rate in the stimulated reservoir and the efficiency of hydraulic stimulation operation (Maxwell, 2011; Maxwell et al., 2008). In addition, it serves as a qualitative estimate of seismic hazard. Low values of seismic injection efficiency are reported for hydraulic fracturing, and high efficiencies are attributed to stimulations that activate preexisting reservoir faults (Maxwell, 2013), leading to additional release of stored tectonic stresses. The analysis of full seismic moment tensors reveals the amount of volumetric and shear strain during faulting and allows to infer the respective contributions from fracture opening and closing and shear displacements (Norris et al., 2016) possibly related to changes in pore fluid pressure (e.g., Fischer & Guest, 2011; Rutledge et al., 2015; Staněk & Eisner, 2017; Zhao et al., 2014) and permeability (Baig et al., 2010, 2015; Martínez-Garzón et al., 2017; Norris et al., 2016; Zhao et al., 2014). Full moment tensors also provide information on fault plane orientations that can be used to calculate the local stress field through stress tensor inversion (e.g., Martínez-Garzón et al., 2013, 2016). Focal mechanisms may also be used to detect the potential of earthquake propagation along preexisting and potentially highly stressed faults leading to large seismic events (e.g., Martínez-Garzón et al., 2016; Walsh & Zoback, 2016; Yeck et al., 2017).

Laboratory (e.g., Charalampidou et al., 2014; Elkhoury et al., 2011; Stanchits et al., 2011) and small-scale in situ experiments (Chitrala et al., 2011; Guglielmi et al., 2015; Warpinski et al., 1999) allow to improve our understanding of the relation between fluid injection operations and the activation of faults and fractures resulting in seismic activity and seismic hazard. In situ experiments in underground laboratories involving seismic monitoring conditions with good coverage of the focal sphere and near the stimulated rock volume allow to close the gap between controlled rock deformation experiments in the laboratory and uncontrolled tectonic processes at plate boundary scale. However, a key element in monitoring the induced microfracturing processes is the detection level of a seismic network, which depends on several factors including appropriate instrumentation (e.g., Kwiatek & Ben-Zion, 2016). Seismic events generated during hydraulic stimulation on reservoir scale display moment magnitudes typically between -3 and 1 (Warpinski et al., 2012), corresponding to rupture sizes from meters to tens of meters. In in situ experiments, detectable events with magnitudes between $M -5$ to -4 result from the activation of microfractures of approximate centimeter size (Kwiatek et al., 2011), approaching the microfractures observed in laboratory experiments with $M_W < -7$ (Goodfellow et al., 2015). It follows that a variety of sensors should be used to monitor the full set of physical processes. To monitor quasi-static processes, strainmeters (Guglielmi et al., 2015) or distributed acoustic sensing are in use. To monitor seismic deformation at small spatial scale (tens of meters to centimeters) and down to magnitudes on the order of $M_W = -4$, only the combined use of broadband seismometers, short-period geophones, high-frequency accelerometers, and acoustic emission (AE) sensors would allow to cover the entire seismic frequency band and thus to explore the full range of dynamic processes and fracture scales (Bohnhoff et al., 2010; Kwiatek et al., 2011; Zang, Stephansson, Stenberg, et al., 2017). Although hydraulic fracturing on in situ scale is a common tool for stress measurements (e.g., Ask, 2006) in mining, the fracture process and associated small-scale brittle rock failure is typically not monitored and analyzed with adequate passive seismic monitoring networks. The feasibility to monitor fracture processes of hydraulic fracturing in situ were demonstrated by Eisenblätter (1988), Niitsuma et al. (1993), and Manthei et al. (2003). The results from recent in situ experiments showed the efficiency of combined seismic monitoring (Gischig et al., 2018; Kwiatek et al., 2011; López Comino et al., 2017; Nakatani et al., 2008; Plenkers et al., 2010).

Table 1
Overview of Selected Stimulation Stages Performed During Hydraulic Fracturing Experiment in Äspö

Stimulation stage	Pressure evolution scheme	Lithology	Injection duration [s]	Median injection pressure [MPa]	Total injected volume [dm³]	Flow rate [dm·s⁻¹]	Fracture breakdown or reopening pressure [MPa]	Total number recorded AE events (no. events after stimulation)	No. moment tensor solutions obtained	Maximum moment magnitude
HF1.0 (frac)	Constant	Ävrö granodiorite	48	11.1	0.8	0.015	13.1	0	—	—
HF1.1			123	9.2	2.6	0.022	8.9	3 (3)	1	−3.8
HF1.2			164	8.4	4.4	0.027	7.7	10 (4)	—	−4.0
HF1.3			122	8.5	5.0	0.042	8.6	12 (3)	2	−3.9
HF1.4			61	8.9	4.6	0.077	8.8	4 (2)	—	−3.9
HF1.5			118	8.8	9.2	0.078	8.2	20 (1)	—	−3.8
HF2.0 (frac)	Constant	Ävrö granodiorite	105	9.3	2.9	0.028	10.9	8 (0)	1	−3.9
HF2.1			181	9.1	5.0	0.028	6.7	6 (5)	—	−3.8
HF2.2			32	8.9	1.2	0.042	7.5	0	—	—
HF2.3			121	9.5	5.1	0.042	6.1	17 (3)	—	−3.8
HF2.4			60	10.0	4.7	0.080	7.1	21 (10)	2	−3.7
HF2.5			120	10.7	9.4	0.080	7.2	50 (16)	5	−3.5
HF3.0 (frac)	Progressive	Ävrö granodiorite	780	progressive (median 3 MPa)	1.6	0.015	9.2	0	—	—
HF3.1	Constant		125	9.7	3.3	0.027	8.8	0	—	—
HF3.2			123	10.1	5.2	0.042	5.9	0	—	—
HF3.3			65	11.1	5.5	0.088	7.7	1 (1)	—	−4.0
HF3.4			120	10.2	10.5	0.088	5.9	14 (0)	—	−3.8
HF6.0 (frac)	constant	Granite	n/a			0.082	11.3	15 (n/a)	17	−3.5

Note. Stimulations 4 and 5 are not listed due to the lack of AE activity. Note that hydraulic data for stimulation HF6 is not available.

Hydraulic fracturing experiment performed in the Äspö Hard Rock Laboratory (HRL), Sweden, resulted in occurrence of seismic activity initially discussed in the context of its spatial and temporal correlation with hydraulic operations (Zang, Stephansson, Stenberg, et al., 2017). In this study we refine and extend the original industrial seismic hypocenter catalog and perform an in-depth study of the spatiotemporal evolution and source characteristics of seismic events with magnitudes M_W ranging from −4.2 to −3.5 (referred to as picoseismicity following Bohnhoff et al., 2010), corresponding to extremely small microfractures of decimeter scale. Source characteristics studied involve event magnitude, radiated energy, and source mechanisms that are then related to fluid injection rate, pressure, and stress field orientation. We discuss the evolution of a microfracture network during and after injection operations and relate the energy budget of hydraulic fracturing operation to the observed seismic response and maximum magnitude.

2. Data

2.1. The 2015 Hydraulic Fracturing Project in the Äspö HRL

A fatigue hydraulic fracturing in situ experiment was performed in the Äspö HRL, Sweden, at a depth of 410 m in 2015. In the following, we summarize the main features of the experiment and refer to Zang, Stephansson, Stenberg, et al. (2017) for details on geology, tectonics, and experimental setup. The stimulated volume consists of igneous rocks forming three adjacent units: the Ävrö granodiorite, a fine-grained diorite-gabbro unit, and a granite unit with an age of about 1.8 Ma (Table 1). Close to the stimulation site, a thrust to transpressional stress regime was estimated using the overcoring method with principal stress magnitudes of S_1 = 22.6 MPa, S_2 = 9.5 MPa, and S_3 = 8.1 MPa and trend/plunge of 312°/3° (S_1), 43°/9° (S_2), and 200°/80°(S_3), respectively (Ask, 2006).

Six hydraulic stimulations were performed in a 28-m-long, horizontal borehole using three different injection schemes (Figure 1; see also Movie S1 in the supporting information). The particular injection interval was selected to omit the existing fractures (fracture density in injection boreholes was approximately 4 m⁻¹)
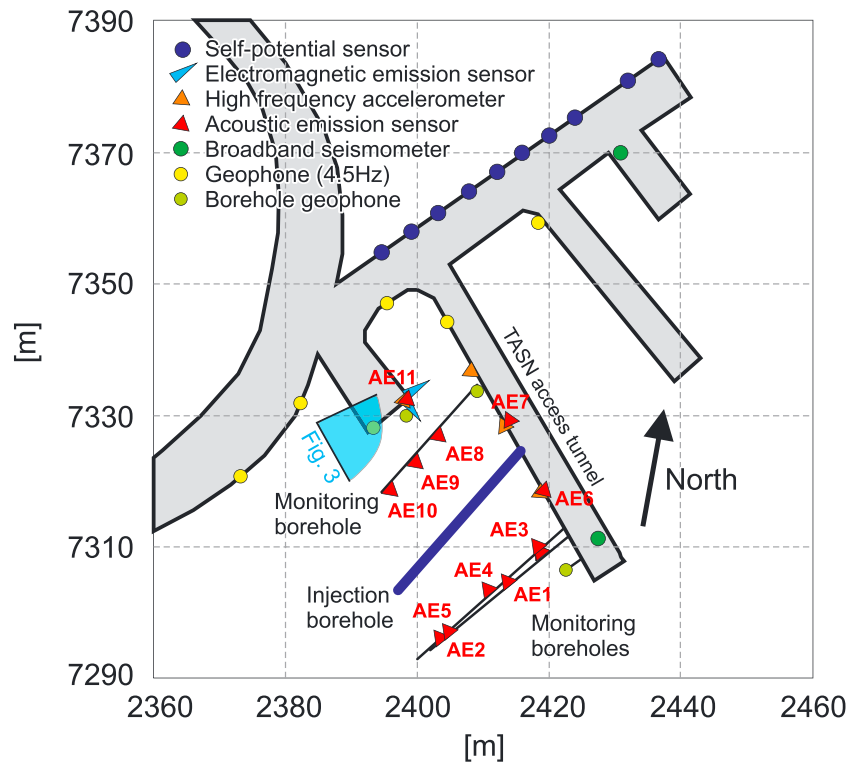
Figure 1. The locations of different seismic and electromagnetic emission sensors in the proximity of injection borehole (more sensors were installed at larger distances, see Figure 4 in Zang, Stephansson, Stenberg, et al., 2017). The high-frequency accelerometers and AE sensors (orange and red triangles, respectively) were located in dedicated boreholes drilled close by the stimulated area. The AE sensors are labeled AE1–AE11. The blue fan shows the camera location and viewing angle of 3-D view presented in Figure 3 (see also Movie S1 in the supporting information). AE = acoustic emission.

detected with borehole camera images (cf. Zang, Stephansson, Stenberg, et al., 2017). Up to 30 dm^3 of fluid (water) were injected during each stimulation at a maximum injection (wellhead) pressure of 13 MPa. Each stimulation was composed of an initial fracturing stage and up to five refracturing stages (cf. Table 1) according to the International Society of Rock Mechanics suggested method (Haimson & Cornet, 2003).

Three stimulations were performed in Ävrö granodiorite, two stimulations in the fine-grained diorite-gabbro, and one stimulation in the fine-grained granite section (Table 1). In this study, we focus on the stimulations HF1, HF2, HF3 (all Ävrö granodiorite), and HF6 (fine-grained granite) during which notable induced picoseismic activity was detected (Figure 2). The initial stimulation stages of HF1.0, HF2.0, and HF6.0 were performed at constant flow rate until the fracture breakdown pressure was reached. In the following refrac stages (HF1.1-5, HF2.1-5, and HF3.1-4), the flow rates were also kept constant but increased progressively in consecutive refrac stages (cf. Figures 2 and S5 in the supporting information). Stimulation HF3.0 was performed following progressive stimulation pressure cycles in which the injection pressure was slowly increased until breakdown pressure was reached. The increase of injection pressure and flow rates was alternated with shut-in stages.

2.2. Seismic Monitoring

The small rock volume of 2,700 m^3 (30 m × 30 m × 30 m) surrounding the injection borehole was monitored by a multisensor network consisting of different independent subnetworks (Zang, Stephansson, Stenberg, et al., 2017). The microseismic network was composed of five broadband seismometers (three-component 120-s Trillium Compact sensors installed in tunnels) and 34 short-period geophones (26 vertical SM6 4.5-Hz geophones located in tunnels and 6 three-component GS13-L3 28-Hz geophones located in boreholes and tunnels). These sensors were located at distances between a few meters and 100 m from the injection borehole. This network was designed to cover the lower seismic frequency band and to ensure proper recording or eventually occurring larger magnitude events. In addition, a high-frequency seismic network combining four high-frequency accelerometers (1C Wilcoxon 736T) and eleven 1C side-view in situ AE sensors (GMuG
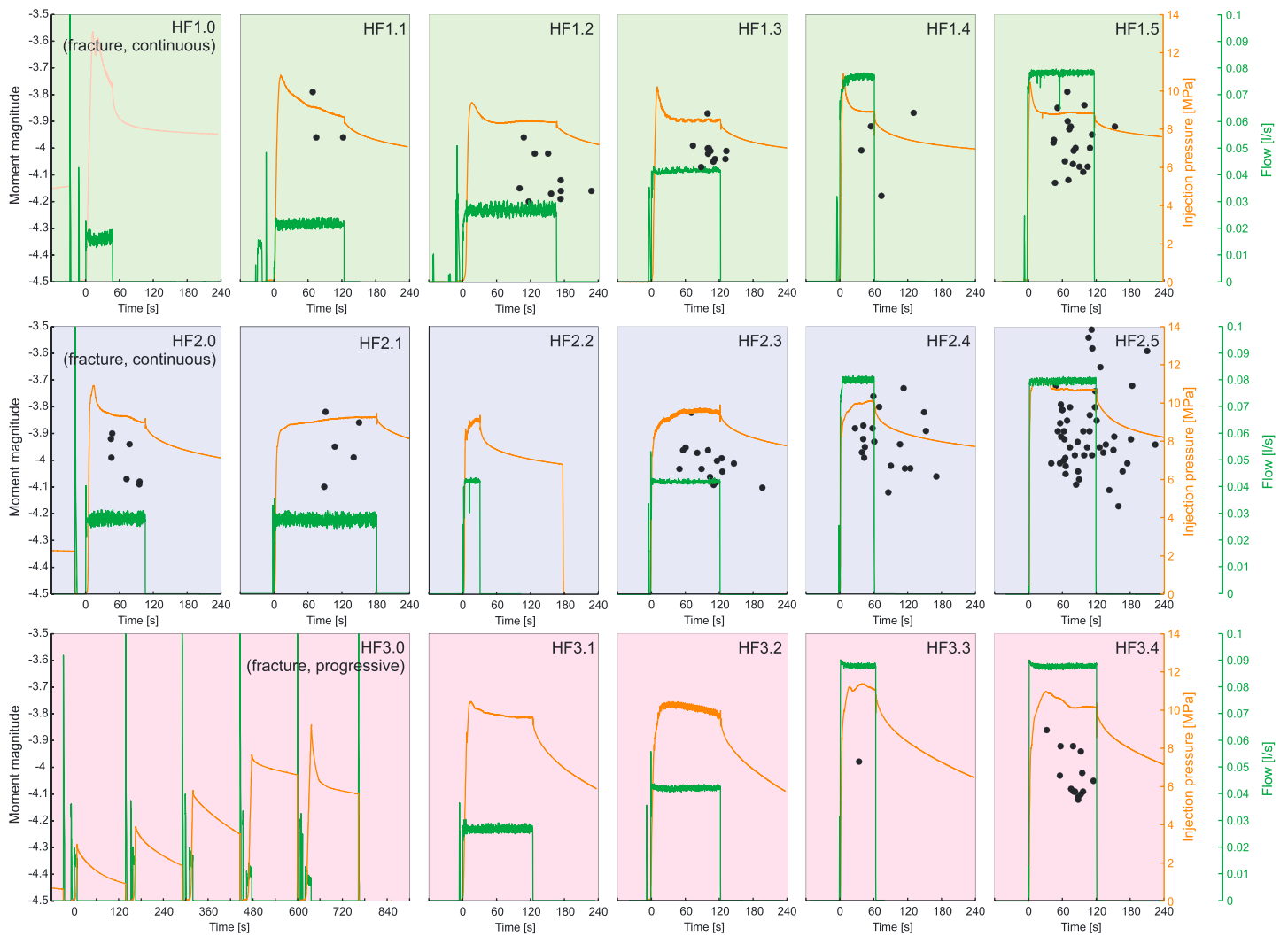
Figure 2. Overview of temporal evolution of injection (wellhead) pressure and fluid flow rate (orange and green lines, respectively) of stimulations HF1–HF3. The seismic activity is plotted with black dots. Note different time scale for stimulation HF3.0.

MA BLw-7-70-75) were installed in dedicated boreholes at a depth of 407 m in direct proximity to the stimulation area (Figure 1; see also Movie S1 in the supporting information). The GMuG 16-channels in situ acquisition system was operating at a 1-MHz sampling rate (one channel was spared for the time synchronization between different networks) in two concurrent modes, namely, continuous recording and triggered recording (with real-time processing involving *P* wave and *S* wave arrival time picking and hypocenter determination). The high-frequency acquisition system covered the seismic frequencies between 50 and 100,000 Hz, thereby allowing to obtain full waveforms of seismic events with moment magnitudes between −5.0 and 0, corresponding to source sizes from meter to centimeter scale (Bohnhoff et al., 2010; Kwiatek et al., 2011; Plenkers et al., 2010).

2.3. Picoseismic Activity

A total of 196 picoseismic seismic events were detected with the high-frequency AE sensors and located in real time during the entire set of hydraulic stimulations. In situ data processing was achieved using an AE software developed by the industrial partner GmuG mbH (see Zang, Stephansson, Stenberg, et al., 2017, for details; Figure 3; see also Movie S2 in the supporting information). Three borehole geophones recorded seismic events associated with the HF3 injection, however, at extremely low signal-to-noise ratio, and no events could be visually observed on the short-period and broadband sensors (cf. Zang, Stephansson, Stenberg, et al., 2017). Finally, the high-frequency accelerometers displayed signatures of waveforms recorded
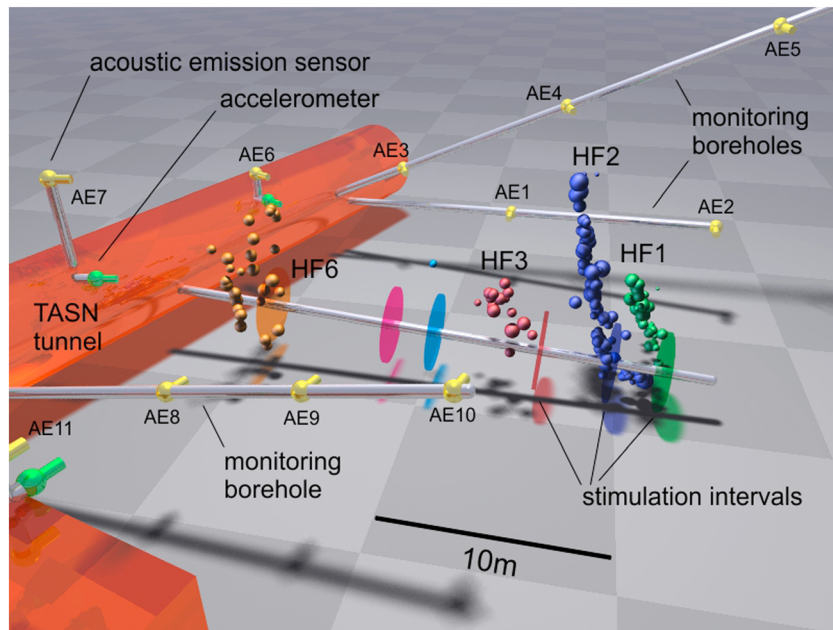
Figure 3. The 3-D visualization of the project site (view from north-west, cf. Figure 1) at 410-m depth. The seismic activity is shown with spheres of various colors reflecting the stimulation stage and size corresponding to the moment magnitude. The schematic position of injection intervals for stimulations HF1–HF6 are presented as semitransparent disks of arbitrary chosen size with the color reflecting the stimulation (from right to left: green—HF1; blue—HF2; red—HF3; teal—HF4; magenta—HF5; and yellow—HF6). The acoustic emission (AE) sensors are marked with labels AE1–AE13. The dimension of the checkerboard pattern is 10 × 10 m. The 1C AE sensors and 1C accelerometers and their orientation are shown along monitoring boreholes using yellow and green bottle-shaped objects.

during the occurrence of 196 AE events, however, at unusable, extremely low signal-to-noise ratio. All signals detected and visually classified as AE events occurred either during the stimulations or shortly (up to 200 s) thereafter during the shut-in phases. In addition, numerous signals have been recorded including hammer hits performed around tunnel walls, signals of various maintenance works typically located around injection borehole collar or other monitoring boreholes, electromagnetic disturbances, and other, undefined noises signals. The signals were classified according to their spatial and temporal occurrence in a detailed field protocol and visual waveform inspection as well as analysis of their frequency-amplitude content (cf. Plenkers et al., 2010).

None of the 196 AE events that were framing stimulation stages were recorded on any of the three available accelerometer sensors with sufficient signal-to-noise ratio to allow for source analysis. However, signals from local hammer hits performed along the tunnel walls prior to the fluid injection, as well as underground work-related impulsive signals occurring in-between stimulation stages were successfully recorded on both types of instruments allowing for sensor cross-calibration (see supporting information Text S1).

2.4. Data Processing and Refinement

The initial seismicity catalog containing 196 fully automatically located AE events was here manually reprocessed to further refine the accuracy of the automatic picks and subsequent hypocenter locations. This resulted in a significant increase in the number of P wave and S wave onset times by 35% (1,760 P wave arrivals) and 700% (1,206 S wave arrivals), respectively. In the next step, the absolute earthquakes locations were determined using P and S wave arrival times. We used a hypocenter determination algorithm based on the equivalent differential time method (location method; Font et al., 2004; Lomax, 2005; Zhou, 1994) and the Metropolis-Hastings Random Walk sampler for obtaining the final hypocenter location and uncertainty estimation (e.g., Hastings, 1970; Metropolis et al., 1953). We used velocity model in which initial information on P wave and S wave velocities was derived from averaged ultrasonic velocity measurements performed along injection borehole (Zang, Stephansson, Stenberg, et al., 2017), resulting in assumption of V_P = 5,800 m/s and V_S = 3,200 m/s for the entire investigated rock volume ($\frac{V_P}{V_S}$ = 1.81). These velocities were in good

agreement with the V_P/V_S ratio obtained from Wadati diagram (Wadati & Oki, 1933) using P wave and S wave arrivals of AE events. Finally, the velocity model was validated by comparing known locations of hammer hits with locations derived from inversion of P wave and S wave onset times of hammer signals.

To increase the precision of the source locations, the AE events were relocated using the double-difference relocation technique (Waldhauser & Ellsworth, 2000). The relocation uncertainties were estimated using bootstrap resampling (e.g., Harrington et al., 2015; Waldhauser & Ellsworth, 2000). With this approach, the initially reported maximum hypocenter location residual of 0.3 m (Zang, Stephansson, Stenberg, et al., 2017) was further reduced, resulting in relative precision of hypocenter determination of approximately 0.1 m. With this the original locations were further improved now enabling tracing the spatial and temporal evolution of picoseismicity in much greater detail.

In addition to onset times, P wave first-motion polarities, amplitudes, and rise times were determined. For events with best available S/N ratio we performed double-couple constrained moment tensor (DCMT) and full moment tensor (FMT) inversions using the hybridMT software package (Kwiatek et al., 2016). The seismic FMTs and DCMTs were initially calculated for 28 out of the 196 AE events (mostly events from stimulation HF6 and a few events from stimulations HF1 and HF2, cf. Table 1). To further improve the quality of the calculated MTs, we used the hybrid moment tensor approach (Andersen, 2001; Kwiatek et al., 2016; see also Martínez-Garzón et al., 2017). This allows suppressing the influence of propagation and site effects on resulting MTs. The refinement was performed independently for two well-separated spatial seismicity clusters consisting of selected events recorded during stimulations HF1–HF3, and stimulation HF6, respectively (cf. Figure 3). To evaluate the uncertainties of FMTs and DCMTs, we repeated the MT inversions 100 times using perturbed input amplitude data (Figure S4). For each perturbed input data set, we randomly modified the input P wave amplitudes up to 10%, and the takeoff angles (±6°), simulating the influence of noise/site and velocity model uncertainties (cf. Martínez-Garzón et al., 2017; see also Davi et al., 2013). In 7 cases, the resampled MT solutions display ambiguous focal mechanism orientations, reducing the number of reliable MTs to 21. For these remaining events we compared root-mean-square errors of FMTs and DCMTs using Bayesian Information Criterion technique (Cesca et al., 2012). We found that in 17 cases the reduction in root-mean-square error of FMTs can be likely explained by increased number of free moment tensor components from 4 to 6 (see supporting information Figure S6 for details on the procedure). Therefore, in the following discussion we used the DCMTs and values of isotropic components of four reliable FMTs.

Low-frequency hammer hits recorded on both accelerometers and AE sensors were used to cross-calibrate the AE sensors to actual ground motions in an attempt to estimate AE moment magnitudes. The calibration relied on finding the regression relation between the observed maximum amplitudes at AE sensors and seismic radiated energy estimated from accelerometers (cf. various calibration schemes in Kwiatek et al., 2010, 2011). The details of the calibration procedure are presented in the supporting information Text S1. The estimated moment magnitudes of the AE events ranged between M_W −4.2 ± 0.3 and −3.5 ± 0.3.

Since only a small number of reliable focal mechanisms could be determined, standard fault plane-based stress tensor inversion could not be applied. However, taking advantage of the large number of AE events with reduced number of polarities it is possible to determine directly the stress field orientation from first motion polarities (e.g., Ickrath et al., 2015). Therefore, a nonlinear stress tensor inversion was performed using the MOTSI software (Abers & Gephart, 2001) inverting P wave polarities of the set of AE events to determine the deviatoric stress tensor in the vicinity of stimulation intervals. The stress tensor inversion provided the orientation of the three principal stress axes and the stress ratio coefficient. We aggregated polarity data from four stimulation stages HF1.3, HF1.5, HF2.4, and HF2.5, which were characterized by comparable injection rates and injection pressures. The aggregated polarity data were then divided into two subsets. First subset contained polarities of AE events that occurred during active injections in aforementioned stages (in total 70 AE events with 442 first P wave polarities) and the second one the polarities from AE events following each selected stimulation (comprising 26 events and 163 P wave polarities). The aim of this procedure was to derive and compare the stress field orientation during high injection rates and during the shut-in phase. This way, the resulting inversion provides average stress tensor orientations from four similar stimulations.

The magnitude of completeness of the resulting seismicity catalog and the Gutenberg-Richter b value were calculated using all available AE events. To calculate them, we applied a goodness-of-fit method assuming that at least 90% of data follow the Gutenberg-Richter power law (Wiemer & Wyss, 2000). We found a high

b value with $b = 2.9 \pm 0.2$, being slightly larger than that estimated by López Comino et al. (2017) and a magnitude of completeness of the seismic catalog of about $M_C = -4.1$ (cf. Figure S1 in the supporting information).

3. Results

3.1. General Characteristics of AE Activity

The initial fracturing stages HF1.0 (continuous) and HF3.0 (progressive) are not accompanied by any AE activity. The initial continuous fractures HF2.0 and HF6.0 resulted in 8 and 15 AE events, respectively (Table 1; Figure 2). In general, refrac stages following the initial fracturing stage display an increasing number of AE events correlating with the increase in the product of injection rate and injection pressure (hydraulic energy). The highest total number of AEs is observed during HF1 and HF2 (Table 1), that is, during stimulations at constant injection pressure. The seismic activity following HF3.0 progressive scheme is observed in the later stages HF3.3 and HF3.4, resulting in 1 and 14 events, respectively (Figure 2). The stimulations HF4 and HF5 did not result in occurrence of any detectable AE event (see overview in Zang, Stephansson, Stenberg, et al., 2017).

In the following, we focus on the stimulations resulting in >10 AE events with waveform data displaying high signal-to-noise ratio, thus allowing calculation of source characteristics. These include continuous stimulations HF1, HF2, HF3, and HF6 (cf. Figure 2 and Table 1). Note that in this study we focus on AE events that were detected and located in situ using the AE acquisition system operating in triggering mode optimized for real-time processing. In addition, seismic events with even smaller amplitudes could be detected by full waveform detection and earthquake location algorithms (López Comino et al., 2017) using the data from an additional AE acquisition system operating in continuous mode.

For each analyzed stimulation stage, the first AE events are observed with 30- to 120-s delay after pumping started. In general, AE activity is mostly observed during fluid injection. In addition, refrac stages HF2.4 and HF2.5 show significant seismicity after shut-in of the injection well. In all refrac stages, AE activity occurred at injection wellhead pressures of about 8 MPa in good agreement with the minimum stress estimate from overcoring performed by Ask (2006; cf. Figures 2 and S2).

The AEs radiated during or shortly after a particular stimulation stage display hypocenters within a distance less than 9.5 m from the center of the corresponding injection interval (Figures 4 and S5 and Movie S2). The AE hypocenters recorded during stimulation stages HF1, HF2, HF3, and HF6 mostly occur above the corresponding injection interval (Figure 3). For HF1, HF2, and HF6 the AE hypocenters localize on clearly separated and steeply dipping (about 80°) planar structures oriented roughly perpendicular to the axis of the injection borehole (Figure 3). The structures are significantly elongated in the vertical direction. We estimate a fractal dimension $d = 1.71 \pm 0.17$ (box counting/Minkowski-Bouligand dimension) from aggregated relocated hypocenter data of stimulations HF1 and HF2. The azimuths of the subplanar structures delineated by events from HF1 and HF2 stages are similar (306°). For HF6, the strike of the subplanar structure is approximately 315°. Generally, the strike of all planar event clusters is roughly in the direction of maximum principal stress (maximum horizontal stress; Ask, 2006).

3.2. Source Properties and Seismic Efficiency

Estimated moment magnitudes of AE events that occurred during the stimulations range from $M_W -4.2 \pm 0.3$ to -3.5 ± 0.3. Assuming a static stress drop of 1 MPa and a penny-shaped crack geometry, the M_W range corresponds to fault sizes of 10 to 30 cm in diameter (Eshelby, 1957). Events with such small magnitudes have been reported in the Mponeng South African gold mine (Kwiatek et al., 2010, 2011). Compared to studies from the South African mines (e.g., Kwiatek et al., 2011; Plenkers et al., 2010), we find indications that attenuation is generally stronger in the Äspö HRL. The high-frequency content of waveforms is more strongly depleted compared to events observed in Mponeng although source-receiver distances are similar in both cases. Likely, stronger attenuation is related to much lower confining stresses at Äspö, so existing cracks and joints are less effectively closed compared to almost 10 times larger depth in the Mponeng mine.

Seismicity induced during HF2 stimulation stages shows a progressive increase of maximum event magnitude (and total seismic moment) with total injected fluid volume ΔV and total hydraulic energy $E_I = \overline{P} \times \Delta V$
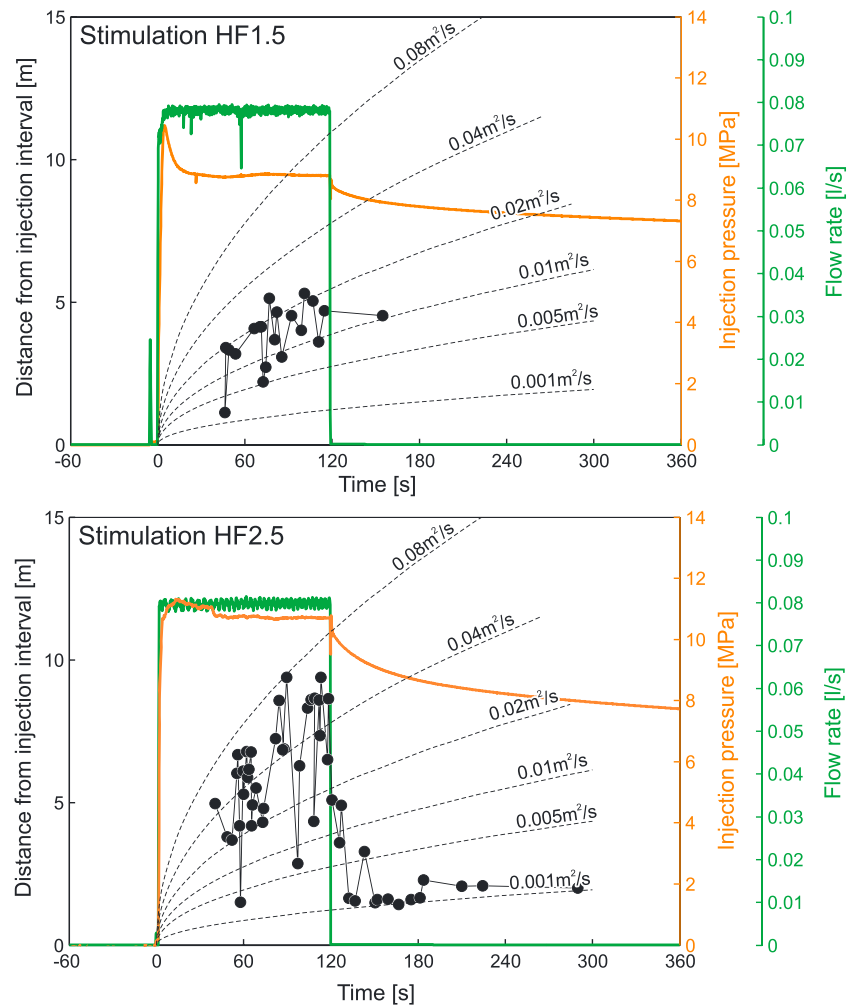
Figure 4. Dependence between the time since the beginning of stimulation and distance of AE events from injection interval for the fifth stage of first and second stimulations (HF1.5 and HF2.5). The AE events are shown as black circles. The injection pressure and fluid flow rate are presented as solid orange and green lines, respectively. The dashed black curves represent expected space-time evolution of a fluid pressure perturbation front triggering seismicity assuming that it is solely controlled be scalar fluid pressure diffusion in a homogeneous isotropic medium (Shapiro et al., 2002, eq. 6; see discussion in the text). The dashed curves are parameterized using different values of apparent hydraulic diffusivities.

supplied using an average injection pressure $\overline{P}$ (Figure 5a). This observation is in contrast to seismic activity monitored during stimulation HF1 where the correlation between maximum event magnitude and hydraulic energy supplied during injection is less clear.

Radiated seismic energy of the AEs was estimated directly from seismic moment (Hanks & Kanamori, 1979; see also supporting information Text S1). Seismic injection efficiency (Maxwell, 2011, 2013; Maxwell et al., 2008) is the ratio E_0/E_I of cumulative radiated seismic energy E_0 and hydraulic energy E_I (Figure 5b). The total injection efficiencies range from 3×10^{-6} (HF3) to 8.5×10^{-6} (HF2); see Figure 5b. In general, the observed values of seismic injection efficiencies ($\sim 10^{-5}$) are significantly lower than the seismic efficiency reported for tectonic earthquakes ($\sim 10^{-2}$). The obtained values are similar or slightly larger compared to seismic injection efficiencies observed by Maxwell et al. (2008) in numerous hydraulic fracturing operations. Seismic injection efficiencies aggregated for each stimulation (rhombs in Figure 5b) are also generally comparable with the seismic injection efficiency of HF3 being smaller by a factor ~ 3 from the seismic injection efficiency of HF2. Interestingly, the cumulative radiated energy E_0 was found to increase with hydraulic energy rate for stimulations HF1 and HF2 (Figure 5c).
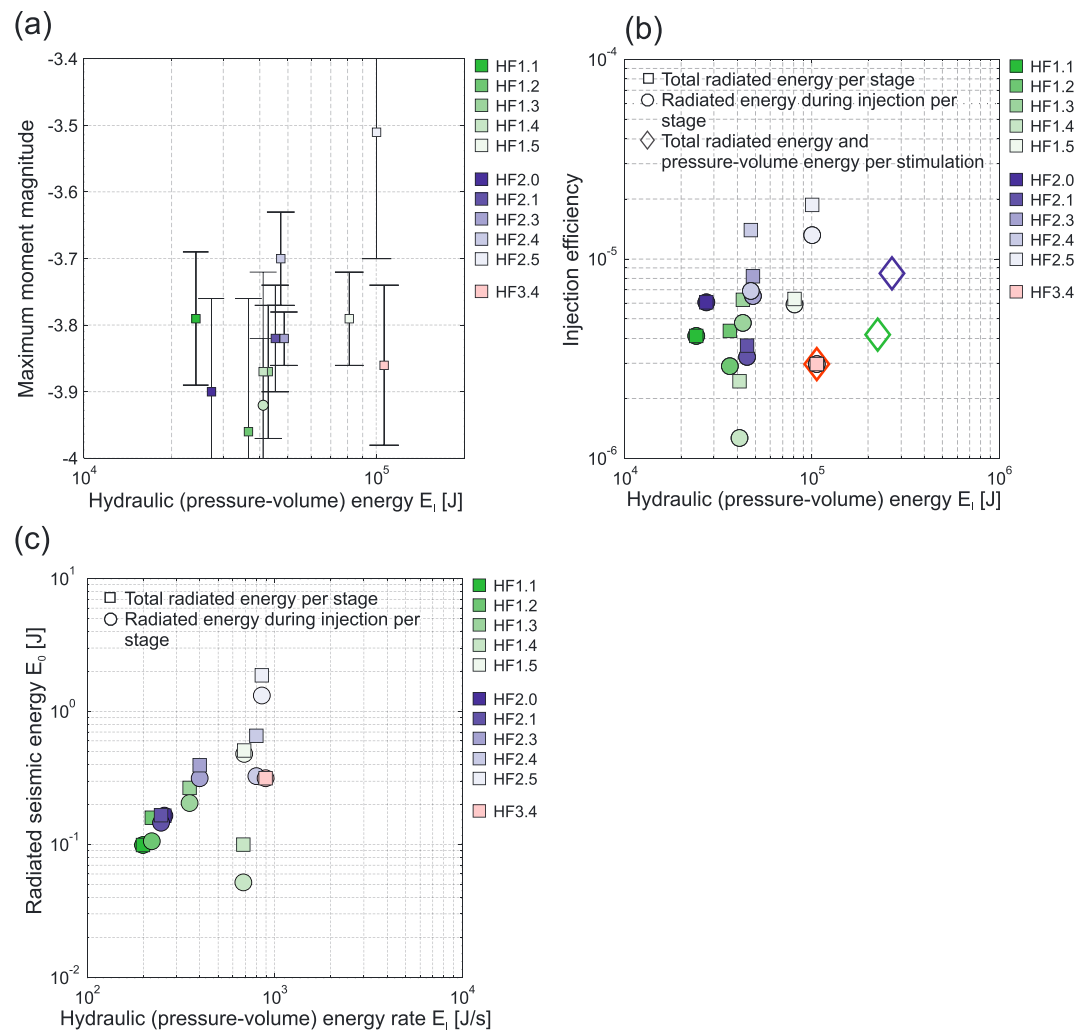
Figure 5. (a) Relation between hydraulic energy (pressure-volume) and maximum moment magnitude in the stimulation stages HF1, HF2, and HF3. The uncertainties correspond to 2 times the mean absolute deviation. (b) Relation between hydraulic energy E_I and seismic injection efficiency (E_0/E_I) for each stimulation stage. The square and circle symbols correspond to seismic injection efficiency calculated as a sum of E_0 of all events, and those occurring only during active stimulation, respectively. The rhomb symbols indicate seismic injection efficiency calculated using cumulative radiated energy of all events occurring during particular stimulation divided by corresponding hydraulic energy for the whole stimulation. (c) Relation between the hydraulic energy rate and radiated seismic energy for each stimulation stage.

3.3. Spatiotemporal Evolution of AE Activity and Source Mechanisms

The spatial and temporal migration of the AE activity observed in selected stages of stimulations HF1 and HF2 provides some insight into the propagation of a progressively forming fracture network. In general, we observed a migration of AE hypocenters away from the injection interval and an upward expansion of the cloud of seismic events (Figure 4; see also Figure S5). A similar AE migration pattern is indicated in other stimulation stages, but it is less clearly observed due to the smaller number of AE events. The expansion seems to slow down or stop after shut-in of injection. For HF2.4 and HF2.5, we observed a collapse of AE hypocenters toward the HF2 injection intervals along the borehole (Figure 3). In addition, in stimulation HF2 it seems that seismicity propagates along two different directions. Most AE hypocenters expand upward, but some events migrate horizontally toward the injection interval of HF1 possibly indicating leakage of the borehole packers enabling communication with previous HF1 stimulation (Zang, Stephansson, & Zimmermann, 2017).

With the exception of refract stages HF2.3 and HF2.4, subsequent refrac stages of stimulation HF2 result in AE activity that seems to occur mostly at progressively larger distance to the injection interval (Figure S5). This
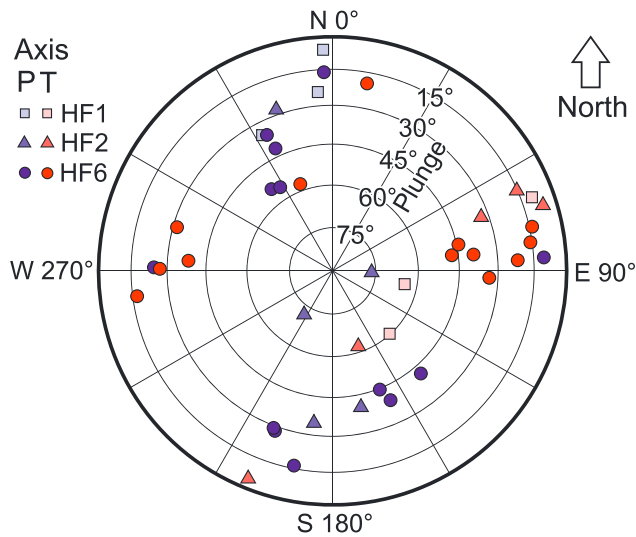
Figure 6. Stereographic equal-area plot of *P* and *T* axes (blue and red symbols) of derived 21 double-couple seismic moment tensors (cf. Figures 1, 3, and S4). Plunges of 0° and 90° correspond to horizontal and vertical directions of *P/T* axes, respectively.

suggests that the stimulated volume surrounding the injection may progressively increase during stimulation. In contrast to stimulations HF1 and HF2, the AE hypocenters from stimulation stage HF3.4 show only minor migration away from the injection point at injection pressures and rates comparable to HF2.5 (cf. Figure S5), as well as indications for complex fracture propagation as documented by impression packer results (cf. Zang, Stephansson, Stenberg, et al., 2017). Due to the lack of hydraulic data, we cannot address the spatiotemporal evolution of AE activity for stimulation HF6.

3.4. Focal Mechanisms and Stress Field

Out of the 196 AE events we could calculate 21 stable seismic DCMTs (Figure S4). Maximum errors of the moment tensor components were calculated from the diagonal elements of the moment tensor covariance matrix (Kwiatek et al., 2016; Martínez-Garzón et al., 2017) and represent <10% of the total seismic moment. The AE events display heterogeneous mechanisms and kinematics (cf. Figures S3–S4), although the *P* and *T* axes tend to cluster (Figure 6), signifying a similar far-field transpressional stress field. In general, fault plane orientations from focal mechanisms are not aligned with the planar trend defined by the AE hypocenters (see Figures S3 and S4 in the supporting information). This suggests that fluid injections resulted in formation/activation of a complex fracture network rather than that of a single, subplanar fracture. In addition, we note that four FMT mechanisms indicated as reliable by the applied Bayesian Information Criterion display minor tensile components (%ISO < 15%, cf. Figure S6 for details).

The state of stress estimated from overcoring measurements (Ask, 2006) is represented in a Mohr circle diagram (Figure 7). We assume that the strength of the rock mass surrounding the injection borehole is limited by ubiquitous fractures and joints with a friction coefficient of 0.85 taken from laboratory experiments and that pore pressure is approximately hydrostatic, which at the depth of 400 m corresponds to 4 MPa. We calculated the fault instability coefficient for 21 stable fault plane solutions and selected the respective nodal
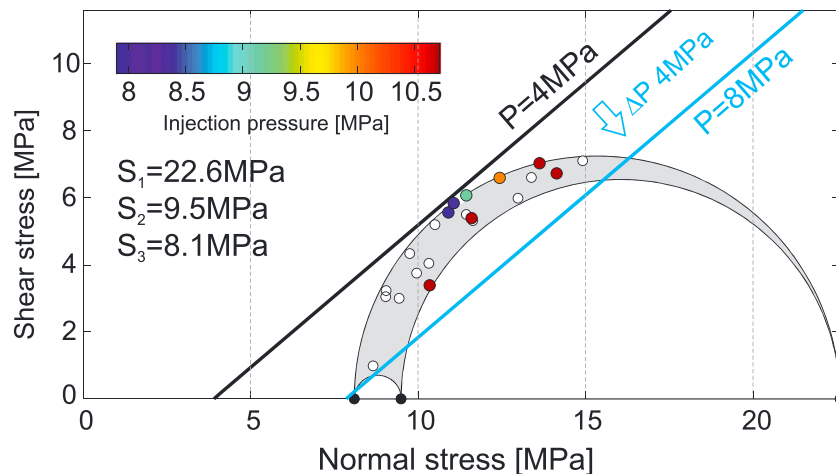

Figure 7. Mohr circle representation of the state of stress in the vicinity of project. The magnitudes of principal stress axes are taken from Ask (2006; assuming density of 2,700 kg/m^3, the overburden stress is expected to be 10 MPa at the depth of experiment). The thick black line denotes failure envelope assuming 4 MPa pore fluid pressure and friction coefficient 0.85. Colored dots represent projections of fault planes of 21 AE events on the Mohr circle. For projection we used only the nodal plane that was located closer to the failure envelope (i.e., the one that display higher fault instability coefficient [Martínez-Garzón et al., 2016; Vavryčuk, 2014]). The circle color reflects the injection pressure at the time of AE event occurrence (with white color denoting no information available for injection pressure due to lack of hydraulic data in stimulation HF6).
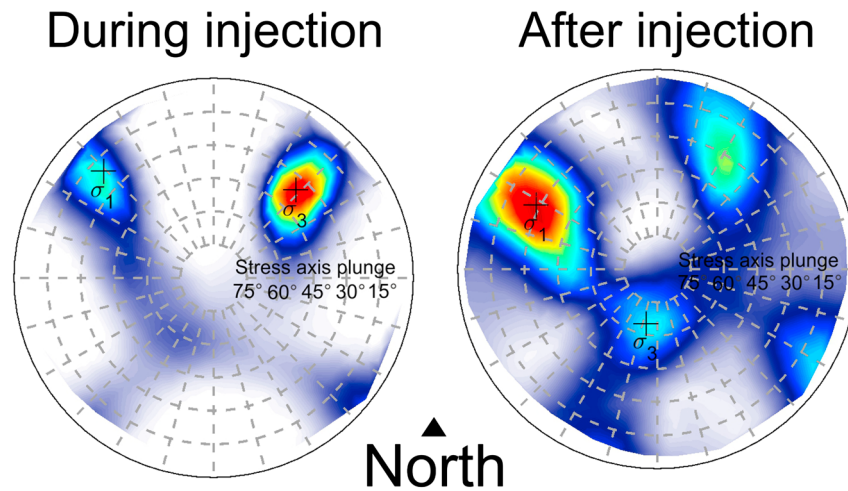
Figure 8. Stress tensors derived from aggregated polarity data using AE events occurring (a) during active injection and (b) after stimulation. The color in stereonets represent the likelihood function of S_1 and S_3 orientation (with warmer color denoting most likely direction of minimum and maximum stress axes). Plunges of 0° and 90° correspond to horizontal and vertical directions of stress axes, respectively.

planes favorably oriented for slip in the local stress field (for details see Martínez-Garzón et al., 2016; Vavryčuk, 2014). Interestingly, the estimated stress states for favorably oriented nodal planes of most events projected on the Mohr circle diagram suggest that they are critically stressed (i.e., located close to the failure envelope), despite of apparent heterogeneity in the kinematics represented by the mechanisms. An additional pore pressure increase of about 4 MPa (8 MPa local pore pressure level, blue line in Figure 7) is sufficient to activate all of the displayed fault planes. Such a pore pressure increase is below the maximum wellhead pressures reached during the stimulation stages. Interestingly, four AE events that occurred at the highest injection pressures occurred on less favorably oriented fault planes with respect to the estimated stress field (dark red dots in Figure 7).

The stress tensor orientations obtained from inverting polarity data of AE events (Figure 8) from both subsets suggests a reverse- to transpressional stress state and are in general agreement with the stress field obtained from overcoring (Ask, 2006). However, only one principal stress axis is well constrained (σ_3 and σ_1, respectively, for time periods during and after injection), whereas the remaining axes are not, reflecting a relatively similar magnitude of the stresses S_2 and S_3 and/or scarcity of input data The stress field orientations calculated from aggregated polarity data of events monitored during injection and after shut-in show a similar orientation. However, the orientations of the intermediate stress σ_2 and minimum stress σ_3 are reversed, indicating a transition from reverse faulting to a strike-slip regime during active stimulation.

4. Discussion

Tracking the spatial, temporal, and source characteristics of decimeter scale microfractures activated during hydraulic stimulations is a challenging task due to the high frequency of the emitted seismic waves and attenuation. This requires good network coverage of sensors with high sensitivity in the kilohertz range in close proximity to the injection point. As demonstrated, local high-frequency monitoring using in situ AE sensors allows to record and locate picoseismicity. A combined network incorporating in addition high-frequency accelerometers allows to calibrate in situ the AE sensors and to perform in-depth studies of seismic efficiency and energy budget of hydraulic stimulations. Our results confirm that in situ AE sensors (frequency range 1–100 kHz) have a significantly higher sensitivity than the high-frequency accelerometers used in Äspö in the frequency range 1–25 kHz.

Here we successfully recorded events with magnitudes between M_W −4.2 and M_W −3.5 resulting from hydraulic stimulations performed in Äspö underground laboratory into a small volume of rock at well-defined stress conditions. Our study of induced high-frequency seismicity allows analyzing the complex processes governing hydraulic fracture formation and the resulting implications for seismic hazard assessment and
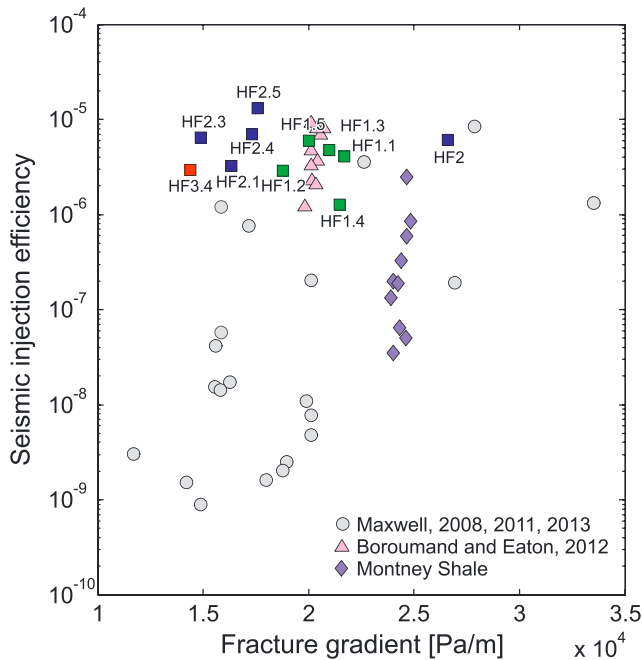
Figure 9. The dependence between fracture gradient and injection seismic efficiency calculated as a ratio of total radiated seismic energy over hydraulic energy E_0/E_I (modified after Maxwell, 2013).

bridge the gap that exists between (industrial) reservoir and laboratory scale experiments. In the following, we elaborate in detail on two of the key findings from this study.

4.1. Seismic Injection Efficiency and Maximum Earthquake Magnitude

The relation between radiated seismic energy of induced events and injection parameters is a matter of current debate (Dieterich et al., 2015; Galis et al., 2017; Halló et al., 2014; McGarr, 2014). However, despite a plethora of microseismic mappings of large-scale reservoir stimulations so far, no robust correlations exist between injection rate, injection volume, and magnitude of seismic events (Maxwell et al., 2015; Warpinski, 2013; Warpinski et al., 2012).

The observed total radiated seismic energy E_0 from the 196 events analyzed in this study amounts to a fraction of 10^{-5} of the hydraulic energy E_I transferred to the stimulated volume by fluid injection (cf. Figure 5b). Considering the large variability between frac and refrac stages, the seismic injection efficiency E_0/E_I is generally on the order of 10^{-5} for the different investigated stimulation stages (HF1, HF2, and HF3.4; see Figure 5b). However, taking into account the large b value observed ($b = 2.9$), significant part of energy may be released by events below the magnitude of completeness of our seismic catalog ($M_C = -4.1$; cf. Halló et al., 2014). Taking a conservative approach, extrapolating the observed Gutenberg-Richter relation (Figure S1) further down to magnitude -6 (fractures of approximate subcentimeter size) would lead to the increase the seismic injection efficiency from 10^{-5} to 10^{-3}. This suggests that the injected hydraulic energy still may be dissipated through some aseismic deformation (as suggested by Maxwell, 2011) and/or slow seismic processes below the frequency and detection band of broadband seismic sensors installed at Äspö (see Zang, Stephansson, & Zimmermann, 2017 for instrumentation details).

Seismic injection efficiencies E_0/E_I estimated for the stimulations HF1-3 are generally somewhat larger compared to efficiencies found for large fracture operations in unconventional reservoirs (Maxwell, 2011, 2013; Maxwell et al., 2008; Figure 9). Maxwell (2011) compared seismic injection efficiencies and frac gradients ∇f (depth-normalized fracture pressures) for hydraulic treatments (for comparison, in Figure 9 we used fracture and refracturing pressures from Zang, Stephansson, Stenberg, et al., 2017, and divided by injection depth of 410 m). High seismic injection efficiencies of the order of up to 10^{-2} were previously attributed to hydraulic stimulations of complex tectonic settings, reactivation of preexisting faults/fractures, and the release of tectonic stresses (Maxwell, 2013) but may also be related to a difference in geologic environments. In extreme cases, seismic injection efficiencies as high as 0.5 were observed in stimulations at Horn River Basin, Canada, and Bowland Shale, UK. These high efficiencies were attributed to triggering of seismicity on preexisting faults (cf. Goodfellow et al., 2015) and the release of tectonic stresses.

The total cumulative seismic moment released in 196 well-defined AE events that occurred during all stimulation phases amounts to 0.35×10^6 Nm. This number corresponds to a single earthquake with moment magnitude $M_W -2.4$ and a source radius of approximately 1.8 m assuming a Brune model and a stress drop of 1.0 MPa (Bohnhoff et al., 2010; Kwiatek et al., 2011). Such a cumulative fault length is significantly smaller compared to the actual spatial extent of the AE hypocenter cloud, which spans up to 9.5-m distance from the injection intervals. This emphasizes that only selected patches of the macroscopically visible seismic clouds were activated during the stimulation treatments. It also suggests that the microseismic hypocenter cloud represents a complex fracture network rather than a single planar fracture as has also been suggested previously from microseismic mapping of large-scale reservoir stimulations (Cipolla et al., 2011). Therefore, we suggest that the injected fluids penetrated the borehole wall and propagated further into a preexisting fracture network resulting in the observed distribution of seismic activity.

We assume that subsequent stimulations resulted in an expansion of the damaged rock volume and a permeability enhancement of the activated fracture network. Using the conservative approach of
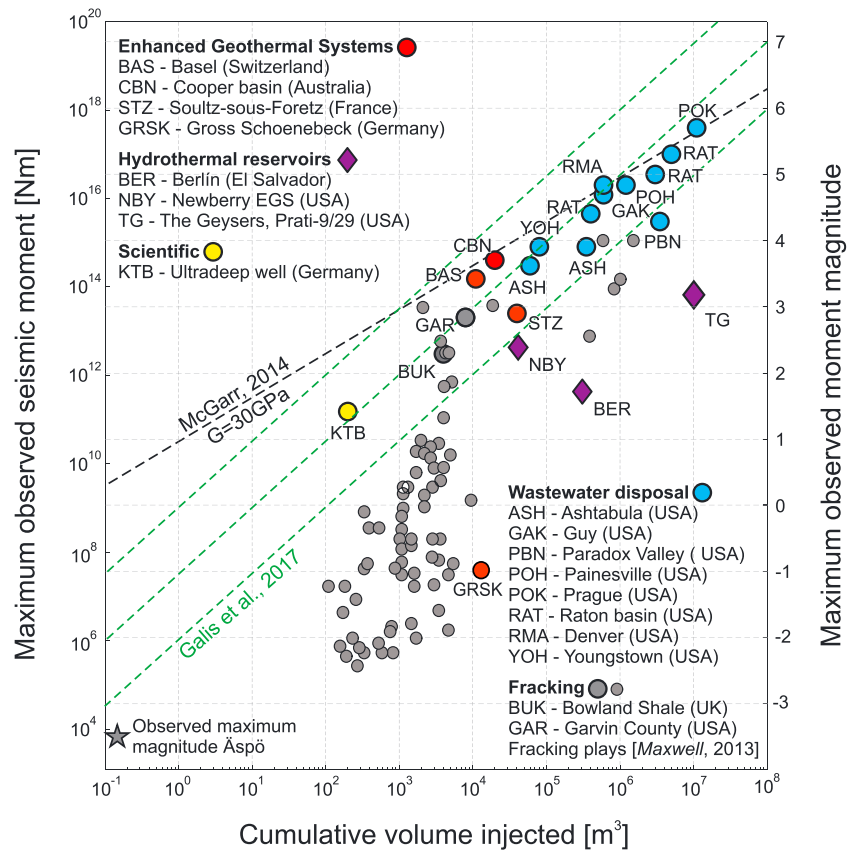
Figure 10. Relation between cumulative volume of fluid injected and maximum observed seismic moment for a number of sites including wastewater disposal, geothermal, fracking, and scientific projects (circles adapted from McGarr, 2014 and rhombs from Kwiatek et al., 2015). The commonly imposed theoretical limit to maximum magnitude assuming shear modulus of 30 GPa is indicated by the dashed black line. Three dashed green lines correspond to relation between maximum magnitude and cumulative volume injected as predicted by Galis et al. (2017) assuming different parameters.

Shapiro et al. (2002) and ignoring poroelastic coupling effects, we find that the apparent hydraulic diffusivity D increased between refrac stages HF2.3, HF2.4, and HF2.5 from $D < 0.01$ m^2/s to $D = 0.08$ m^2/s (Figure S5). Also, in stimulation stages of HF1, apparent hydraulic diffusivity increased from $D = 0.01$ m^2/s to $D = 0.03$ m^2/s but with an overall lower AE activity. The obtained values of hydraulic diffusivity coefficients are similar to values inferred for stimulations of hydrocarbon and geothermal reservoirs, as, for example, in Fenton Hill ($D = 0.17$ m^2/s) and Soultz-sous-Forets ($D = 0.05$ m^2/s), respectively.

We also observed for stimulation stages HF1, HF2, and HF3.4 that the total radiated seismic energy released during injection and after shut-in increased with hydraulic energy rate dE_I/dt (Figure 5c). This suggests that propagation of induced seismicity away from the injection interval and growth of a seismic event cloud and of the stimulated volume may require increasing pumping rates and wellhead pressures (hydraulic energy). This is conceivable, since hydraulic diffusivities of the activated volumes increased with injection cycles. This is expected to result in larger leak-off and, for a fixed injection rate, leading to smaller poroelastic stress perturbations with distance to the injection interval for constant injection rates.

The total volume injected into the rock mass during all stimulation phases is approximately 125 dm^3. McGarr (2014) derived an analytical relation estimating the upper limit to the magnitude of seismic events resulting from injection of a certain volume of fluids ΔV into the reservoir, $M_0^{max,McGarr} = G\Delta V$, where G is rock shear modulus. The relation holds well for a number of case studies including wastewater disposal and EGS sites (Figure 10). However, significant discrepancies have been reported between the theoretical upper limit and the actually observed magnitudes for a number of fracking operations (Maxwell, 2013), EGS sites (Zang et al., 2014), as well as for hydrothermal systems (Kwiatek et al., 2015).

Using $G = \rho V_S^2 = 2,700 \times 3,200^2 = 27.6$ GPa, the expected upper limit to the maximum magnitude due to the injection of 0.125 m^3 of fluids into the rock mass is $M_0^{max,McGarr} = 3.45 \times 10^9$ Nm. This predicts a significantly larger moment magnitude $M_W^{max,McGarr} = 0.29$, compared to the maximum observed moment magnitude ($M_W^{max,obs} = -3.5$), or even the total cumulative seismic moment corresponding to a single earthquake with a M_W -2.4.

For a particular fault and pore pressure perturbation from cumulative fluid injection Galis et al. (2017) estimate a critical moment beyond which a rupture will become unstable. Below this value the rupture is expected to stop spontaneously ("arrested rupture"). The authors derived a model estimating the moment of the largest arrested seismic event, $M_0^{max,arr}$, as a function of cumulative injected fluid volume (Figure 10). They found a steeper slope (1.5) compared to McGarr's model (slope 1) estimating maximum possible magnitude (McGarr, 2014). While for large injection volumes the difference between the two models is minor, for low injection volumes, the predicted event magnitudes differ more significantly. The model of Galis et al. is in better agreement with our data.

Halló et al. (2014) emphasized the importance of aseismic deformation and introduced a seismic efficiency ratio (SER) coefficient that reduces the seismic moment release due to volume change predicted by McGarr (2014) by a scalar factor. For example, for granitic rocks Halló et al. (2014) propose an SER factor of order ~0.1 (cf. Table 2 in Halló et al., 2014). However, the very low seismic moment release and $M_W^{max,obs}$ found in our study would suggest a far smaller SER factor (Figure 10).

Broadband sensors installed in the near field of the experiment in tunnel TASN at Äspö recorded tilt signals already with the first initial fracking (HF2.0), indicating a reopening of an older existing fracture. In contrast, in HF1.0 and HF3.0 no tilt was found during the initial stages, but with the first refrac stage, possibly indicating the creation of one or more new fractures in the initial stage. The existing tilt signals possibly represent quasi-static low-frequency opening and closing of fractures during stimulation (Milkereit et al., 2017; Zang, Stephansson, Stenberg, et al., 2017, Figure 11) recorded only by the broadband sensors but not captured by the AE network. These observations suggest that slow or aseismic deformation partly accommodated stimulations and refrac operations but were not captured by the most sensors of the monitoring networks in Äspö.

4.2. Fracturing Processes and Stress Field

The microseismic activity from stimulation HF2 shows the progressive evolution of a fracture network in consecutive injection stages (Figure S5 in the supporting information). With increasing injection pressure and fluid volume in consecutive injection stage, the AE activity propagates further away from the injection borehole. Mostly, the events propagate upward toward lower stresses. The observed AE event migration signifies the progressive activation of a permeable fracture network with increasing hydraulic energy (rate) increasing during stimulation. For successive stimulation stages, the AE activity occupies increasing rock volumes. However, the discrepancy between stimulated volume inferred from the seismic cloud and accumulated estimated source size of events increases (cf. López Comino et al., 2017). This supports the contention that during the injection stages a complex fracture network was activated rather than a single coherent fracture formed. The experimental protocol and the available data do not allow to decide clearly whether seismicity induced by refrac stages displays a Kaiser effect (Kaiser, 1953), that is, the occurrence of seismicity only after exceeding the injection pressure of the previous stimulation (Baisch et al., 2002, 2010; Cornet et al., 2007; Kwiatek et al., 2014). However, stimulation stage HF2.2 was performed at a lower median injection pressure than the preceding stage HF2.1 and produced no discernible seismic activity. In contrast, the following refrac stages HF2.3–HF2.5 performed at elevated injection pressures (Figures 2 and S5) produced significant seismic activity.

We obtained double-couple source mechanisms of 21 AE events with stable fault plane solutions. For only four events, the FMT inversion is preferred with respect to the double-couple inversion. These events still display dominantly double-couple components with only minor volumetric components (≤15%). All focal mechanism data from stimulations HF1, HF2, and HF6 show varying fault kinematics (Figure S4), generally unrelated to the elongated and planar trends displayed by the AE hypocenter clouds (cf. Figure S3). The observed heterogeneity of the focal mechanisms is likely related to the structural heterogeneity and the presence of faults at all scales (e.g., Ben-Zion & Sammis, 2003). Presumably, local stress and strain fields are

very heterogeneous affecting earthquake nucleation, rupture propagation, and arrest (e.g., Ampuero et al., 2013; Delouis et al., 2002; Ripperger et al., 2007). The local stress heterogeneity and structural complexity are reflected in the recorded AE events that allow resolving source processes occurring at centimeter-to-decimeter-sized fractures, which is beyond the resolution of typical local seismic networks. Large focal mechanisms variability was observed in mechanisms of submillimeter AE events recorded during laboratory stick-slip experiments on rocks samples (Goebel et al., 2017) and attributed to growing fault zone structural complexity and roughness. Finally, we note that the lack of significant non-double-couple components in the four calculated FMT does not mean that tensile opening of fractures is absent. The tilt signals observed using broadband sensors were attributed to the slow (low-frequency) tensile opening of a fracture, as already indicated in Zang, Stephansson, Stenberg, et al. (2017) and could not be recorded by AE sensors due to bandwidth limitations (>1 kHz).

The fault instability coefficients (Vavryčuk, 2014) were calculated for 21 events. Considering stress tensor orientation and stress magnitudes from overcoring (Ask, 2006), we find that the resolved fault planes are critically stressed (Martínez-Garzón et al., 2016; cf. Figure 7). Critically stressed fault planes are expected to fail at a small pore pressure perturbation. Interestingly, seismic events on faults oriented less favorably for failure (Figure 7) only occurred at elevated injection pressures. The influence of pore fluid pressure inducing failure of nonoptimally oriented faults was previously reported for the seismicity observed in Basel and at The Geysers geothermal field (Martínez-Garzón et al., 2016; Terakawa, 2014; Terakawa et al., 2012). For Äspö, a maximum pore pressure increase of roughly $\Delta P = 4$ MPa due to fluid injection would suffice to cause failure on all observed fault planes, irrespective of their orientation. This is in excellent agreement with the observed range of 8- to 13-MPa injection pressures resulting in seismic activity. The refrac injection pressures typically are of the order of the minimum principal stress estimated by overcoring. Rock hydraulic tensile strength was estimated from the difference between observed breakdown and refrac pressures to be about 4.2 MPa (Zang, Stephansson, Stenberg, et al., 2017). This value is significantly lower than the average tensile strength of Äspö diorite of 14.9 MPa estimated from Brazilian tests (Staub et al., 2004). Therefore, it is conceivable that the stimulation did not always result in creation of the new fracture surfaces but rather caused reactivation of preexisting flaws in the rock mass.

Stress tensor inversion using P wave polarities generally reproduces the stress field orientation derived from independent overcoring measurements (Ask, 2006; Figure 8), irrespective of uncertainties. The stress estimates from overcoring data suggest that the intermediate and minimum principle stresses are very similar and distinctly different from the maximum principle stress ($S_1 = 22.6$ MPa, $S_2 = 9.5$ MPa, and $S_3 = 8.1$ MPa). Orientation of the maximum principle stress remains largely unaffected by injection (Figure 8). However, during injection and after shut-in faulting regimes alternate between strike-slip and thrusting due to the close similarity of intermediate and minimum stress magnitudes. At reservoir scale, such changes between faulting regimes due to fluid injection have been previously observed (Dreger et al., 2017; Martínez-Garzón et al., 2013; Schoenball et al., 2014) and were also suggested by modeling (Jeanne et al., 2015; Ziegler et al., 2017).

5. Summary

This study presents a detailed analysis of the seismic response from multiple small-scale stimulations performed in the Äspö HRL, Sweden, monitored in a broad range of elastic wave frequencies by means of broadband, short-period, and in situ acoustic emission networks. The main conclusions are the following:

1. We successfully tracked the spatial, temporal, and source properties of microfractures of extremely small (picoseismic) events with magnitudes between $M_W -4.2$ and $M_W -3.5$ corresponding to decimeter scale fractures. These events were only recorded because in situ AE sensors with high frequencies up to 100 kHz (thus, sensitive to extremely weak ground motions) were installed in a direct proximity (<20 m) of the stimulation well. The AE system allowed tracking the seismic response due to the hydraulic stimulation in unprecedented detail at controlled conditions, with a resolution close to that available in laboratory injection experiments on rocks samples.
2. The seismic activity within the in situ triggered data set is observed exclusively during active stimulations and up to 300 s after the stimulation stages. The spatiotemporal evolution is visible in selected stages populated with significant number of events and presents dominating upward propagation of fractures from injection interval toward lower confining stresses. The faster and further expansion of AE activity

is visible with each subsequent stimulation stage of HF2 visualizing the enhancement of damage and permeability of the fracture network.

3. A correlation between hydraulic energy and maximum moment magnitude or total seismic moment has been found, as well as between the hydraulic energy rate and total radiated energy in case of HF2. The seismic energy release is low with respect to the injected volume, even considering a partial bias in energy estimates due to missing energy from extremely small events. Low seismic energy release leads to a discrepancy between the observed maximum magnitude and the upper constraint predicted by McGarr (2014). The observed magnitudes fit better to a model incorporating self-arrested ruptures (Galis et al., 2017) or alternatively they signify the influence of aseismic deformation (Halló et al., 2014) and/or slow seismic processes undetectable by installed monitoring system.

4. The observed seismicity patterns, source mechanisms, and ratios of radiated to hydraulic energy suggest that the seismicity mainly occurs due to the reactivation of preexisting fractures. Fracture reactivation rather than fracture opening is in line with the heterogeneity of microfracture orientations derived by seismic moment tensor inversion and indicated by generally low values of isotropic components in four available FMTs.

5. The events occur at differently oriented fault planes that are nevertheless mostly favorably oriented with respect to the stress field and critically stressed. The elevated pore fluid pressures due to injection were sufficient to activate high-frequency events also on less favorably oriented fault planes.

References

Abers, G. A., & Gephart, J. W. (2001). Direct inversion of earthquake first motions for both the stress tensor and focal mechanisms and application to southern California. *Journal of Geophysical Research*, *106*(B11), 26,523–26,540. https://doi.org/10.1029/2001JB000437

Ampuero, J.-P., Ripperger, J., & Mai, P. M. (2013). Properties of Dynamic Earthquake Ruptures with Heterogeneous Stress Drop. In *Earthquakes: Radiated energy and the physics of faulting* (pp. 255–261). Washington, DC: American Geophysical Union. https://doi.org/10.1029/170GM25

Andersen, L. M. (2001). *A relative moment tensor inversion technique applied to seismicity induced by mining*. Johannesburg: Univ. of the Witwatersrand.

Ask, D. (2006). Measurement-related uncertainties in overcoring data at the Äspö HRL, Sweden. Part 2: Biaxial tests of CSIRO HI overcore samples. *International Journal of Rock Mechanics and Mining Sciences*, *43*(1), 127–138. https://doi.org/10.1016/j.ijrmms.2005.05.012

Baig, A., Urbancic, T. I., & Prince, M. (2010). Microseismic moment tensors: A path to understanding growth of hydraulic fractures, in *SPE-137771-MS*, Society of Petroleum Engineers, SPE.

Baig, A., Viegas, G., Gallagher, J., Urbancic, T., & von Lunen, E. (2015). Constraining geomechanical models by using microseismic-derived fractures from source mechanisms. *The Leading Edge*, *34*(8), 912–916. https://doi.org/10.1190/tle34080912.1

Baisch, S., Bohnhoff, M., Ceranna, L., Tu, Y., & Harjes, H.-P. (2002). Probing the crust to 9-km depth: Fluid injection experiments and induced seismicity at the KTB superdeep drilling hole, Germany. *Bulletin of the Seismological Society of America*, *92*(6), 2369–2380. https://doi.org/10.1785/0120010236

Baisch, S., Voros, R., Rothert, E., Stang, H., Jung, R., & Schellschmidt, R. (2010). A numerical model for fluid injection induced seismicity at Soultz-sous-Forets. *International Journal of Rock Mechanics and Mining Sciences*, *47*(3), 405–413. https://doi.org/10.1016/j.ijrmms.2009.10.001

Ben-Zion, Y., & Sammis, C. G. (2003). Characterization of fault zones. *Pure and Applied Geophysics*, *160*(3–4), 677–715. https://doi.org/10.1007/PL00012554.Bohnhoff

Bohnhoff, M., Dresen, G., Ellsworth, W., & Ito, H. (2010). Passive seismic monitoring of natural and induced earthquakes: Case studies, future directions and socio-economic relevance. In S. Cloetingh & J. Negendank (Eds.), *New frontiers in integrated solid earth sciences* (pp. 261–285). Netherlands: Springer. https://doi.org/10.1007/978-90-481-2737-5_7

Bommer, J. J., Oates, S., Cepeda, J. M., Lindholm, C., Bird, J., Torres, R., et al. (2006). Control of hazard due to seismicity induced by a hot fractured rock geothermal project. *Engineering Geology*, *83*(4), 287–306. https://doi.org/10.1016/j.enggeo.2005.11.002

Cesca, S., Rohr, A., & Dahm, T. (2012). Discrimination of induced seismicity by full moment tensor inversion and decomposition. *Journal of Seismology*, *17*(1), 147–163. https://doi.org/10.1007/s10950-012-9305-8

Charalampidou, E.-M., Stanchits, S., Kwiatek, G., & Dresen, G. (2014). Brittle failure and fracture reactivation in sandstone by fluid injection. *European Journal of Environmental and Civil Engineering*, *19*(5), 564–579. https://doi.org/10.1080/19648189.2014.896752.

Chitrala, Y., Moreno, C., Sondergeld, C. H., & Rai, C. S. (2011). Microseismic and microscopic analysis of laboratory induced hydraulic fractures, in *SPE-147321-MS*, Society of Petroleum Engineers, SPE.

Cipolla, C. L., Weng, X., Mack, M. G., Ganguly, U., Gu, H., Kresse, O., & Cohen, C. E. (2011). Integrating microseismic mapping and complex fracture modeling to characterize hydraulic fracture complexity, in *SPE-140185-MS*, Society of Petroleum Engineers, SPE.

Cornet, F. H. (2016). Seismic and aseismic motions generated by fluid injections. *Geomechanics for Energy and the Environment*, *5*, 42–54. https://doi.org/10.1016/j.gete.2015.12.003

Cornet, F. H., Bérard, T., & Bourouis, S. (2007). How close to failure is a granite rock mass at a 5 km depth? *International Journal of Rock Mechanics and Mining Sciences*, *44*(1), 47–66. https://doi.org/10.1016/j.ijrmms.2006.04.008

Davi, R., Vavryčuk, V., Charalampidou, E.-M., & Kwiatek, G. (2013). Network sensor calibration for retrieving accurate moment tensors of acoustic emissions. *International Journal of Rock Mechanics and Mining Sciences*, *62*, 59–67. https://doi.org/10.1016/j.ijrmms.2013.04.004

Delouis, B., Giardini, D., Lundgren, P., & Salichon, J. (2002). Joint inversion of InSAR, GPS, Teleseismic, and strong-motion data for the spatial and temporal distribution of earthquake slip: Application to the 1999 İzmit mainshock. *Bulletin of the Seismological Society of America*, *92*(1), 278–299. https://doi.org/10.1785/0120000806

Dieterich, J. H., Richards-Dinger, K. B., & Kroll, K. A. (2015). Modeling injection-induced seismicity with the physics-based earthquake simulator RSQSim. *Seismological Research Letters*, *86*(4), 1102–1109. https://doi.org/10.1785/0220150057

Dreger, D. S., Boyd, O. S., & Gritto, R. (2017). Automatic moment tensor analyses, in-situ stress estimation, and temporal stress changes at The Geysers EGS demonstration project. In: Proceedings of the 42nd Workshop on Geothermal Reservoir Engineering, Stanford, California, USA, 13–15 February 2017.

Dresen, M. G., Ellsworth, W. L., & Ito, H. (2010). Passive seismic monitoring of natural and induced earthquakes: Case studies, future directions and socio-economic relevance. *New Frontiers in Integrated Solid Earth Sciences*, 261–285.

Eisenblätter, J. (1988). Localization of fracture planes during hydraulic fracturing experiments in a salt mine. In J. Eisenblätter (Ed.), *Acoustic emissions*, (pp. 291–303). Oberursel: DGM Informationsgesellschaft Verlag.

Elkhoury, J. E., Niemeijer, A., Brodsky, E. E., & Marone, C. (2011). Laboratory observations of permeability enhancement by fluid pressure oscillation of in situ fractured rock. *Journal of Geophysical Research*, 116, B02311. https://doi.org/10.1029/2010JB007759

Eshelby, J. D. (1957). The determination of the elastic field of an ellipsoidal inclusion, and related problems. *Proceedings of the Royal Society A: Mathematical, Physical and Science*, 241(1226), 376–396. https://doi.org/10.1098/rspa.1957.0133

Fischer, T., & Guest, A. (2011). Shear and tensile earthquakes caused by fluid injection. *Geophysical Research Letters*, 38, L05307. https://doi.org/10.1029/2010GL045447

Font, Y., Kao, H., Lallemand, S., Liu, C.-S., & Chiao, L.-Y. (2004). Hypocentre determination offshore of eastern Taiwan using the maximum intersection method. *Geophysical Journal International*, 158(2), 655–675. https://doi.org/10.1111/j.1365-246X.2004.02317.x

Galis, M., Ampuero, J. P., Mai, P. M., & Cappa, F. (2017). Induced seismicity provides insight into why earthquake ruptures stop. *Science Advances*, 3(12). https://doi.org/10.1126/sciadv.aap7528

Gischig, V. S., Doetsch, J., Maurer, H., Krietsch, H., Amann, F., Evans, K. F., et al. (2018). On the link between stress field and small-scale hydraulic fracture growth in anisotropic rock derived from microseismicity. *Solid Earth*, 9(1), 39–61. https://doi.org/10.5194/se-9-39-2018

Goebel, T. H. W., Kwiatek, G., Becker, T. W., Brodsky, E. E., & Dresen, G. (2017). What allows seismic events to grow big?: Insights from b-value and fault roughness analysis in laboratory stick-slip experiments. *Geology*, 45(9), 815–818. https://doi.org/10.1130/G39147.1

Goodfellow, S. D., Nasseri, M. H. B., Maxwell, S. C., & Young, R. P. (2015). Hydraulic fracture energy budget: Insights from the laboratory. *Geophysical Research Letters*, 42(9), 3179–3187. https://doi.org/10.1002/2015GL063093

Guglielmi, Y., Cappa, F., Avouac, J.-P., Henry, P., & Elsworth, D. (2015). Seismicity triggered by fluid injection–induced aseismic slip. *Science*, 348(6240), 1224–1226. https://doi.org/10.1126/science.aab0476

Haimson, B. C., & Cornet, F. H. (2003). ISRM suggested methods for rock stress estimation—Part 3: Hydraulic fracturing (HF) and/or hydraulic testing of pre-existing fractures (HTPF). *International Journal of Rock Mechanics and Mining Sciences*, 40(7–8), 1011–1020. https://doi.org/10.1016/j.ijrmms.2003.08.002

Halló, M., Opršal, I., Eisner, L., & Mohammed, A. Y. (2014). Prediction of magnitude of the largest potentially induced seismic event. *Journal of Seismology*, 18(3), 421–431. https://doi.org/10.1007/s10950-014-9417-4

Hanks, T. C., & Kanamori, H. (1979). A moment magnitude scale. *Journal of Geophysical Research*, 84(B5), 2348–2350. https://doi.org/10.1029/JB084iB05p02348

Harrington, R. M., Kwiatek, G., & Moran, S. M. (2015). Self-similar rupture implied by scaling properties of volcanic earthquakes occurring during the 2004-2008 eruption of Mount St. Helens, Washington. *Journal of Geophysical Research: Solid Earth*, 120, 4966–4982. https://doi.org/10.1002/2014JB011744

Hastings, W. K. (1970). Monte Carlo sampling methods using Markov chains and their applications. *Biometrica*, 57(1), 97–109. https://doi.org/10.1093/biomet/57.1.97

Ickrath, M., Bohnhoff, M., Dresen, G., Martínez-Garzón, P., Bulut, F., Kwiatek, G., & Germer, O. (2015). Detailed analysis of spatiotemporal variations of the stress field orientation along the Izmit-Düzce rupture in NW Turkey from inversion of first motion polarity data. *Geophysical Journal International*, 202(3), 2120–2132. https://doi.org/10.1093/gji/ggv273

Jeanne, P., Rutqvist, J., Dobson, P. F., Garcia, J., Walters, M., Hartline, C., & Borgia, A. (2015). Geomechanical simulation of the stress tensor rotation caused by injection of cold water in a deep geothermal reservoir. *Journal of Geophysical Research: Solid Earth*, 120, 8422–8438. https://doi.org/10.1002/2015JB012414

Kaiser, J. (1953). Kenntnisse und Folgerungen aus der Messung von Geräuschen bei Zugbeanspruchung von metallischen Werkstoffen. *Archiv für das Eisenhüttenwesen*, 24(1-2), 43–45. https://doi.org/10.1002/srin.195301381

Kwiatek, G., & Ben-Zion, Y. (2016). Theoretical limits on detection and analysis of small earthquakes. *Journal of Geophysical Research: Solid Earth*, 121(8), 5898–5916. https://doi.org/10.1002/2016JB012908

Kwiatek, G., Bulut, F., Bohnhoff, M., & Dresen, G. (2014). High-resolution analysis of seismicity induced at Berlín geothermal field, El Salvador. *Geothermics*, 52, 98–111. https://doi.org/10.1016/j.geothermics.2013.09.008

Kwiatek, G., Martínez-Garzón, P., & Bohnhoff, M. (2016). HybridMT: A MATLAB/Shell environment package for seismic moment tensor inversion and refinement. *Seismological Research Letters*, 87(4), 964–976. https://doi.org/10.1785/0220150251

Kwiatek, G., Martínez-Garzón, P., Dresen, G., Bohnhoff, M., Sone, H., & Hartline, C. (2015). Effects of long-term fluid injection on induced seismicity parameters and maximum magnitude in northwestern part of The Geysers geothermal field. *Journal of Geophysical Research: Solid Earth*, 120, 7085–7101. https://doi.org/10.1002/2015JB012362

Kwiatek, G., Plenkers, K., & Dresen, G. (2011). Source parameters of picoseismicity recorded at Mponeng deep gold mine, South Africa: Implications for scaling relations. *Bulletin of the Seismological Society of America*, 101(6), 2592–2608. https://doi.org/10.1785/0120110094

Kwiatek, G., Plenkers, K., Nakatani, M., Yabe, Y., Dresen, G., & J. Group (2010). Frequency-magnitude characteristics down to magnitude −4.4 for induced seismicity recorded at Mponeng gold mine, South Africa. *Bulletin of the Seismological Society of America*, 100(3), 1165–1173. https://doi.org/10.1785/0120090277

Lomax, A. (2005). A reanalysis of the hypocentral location and related observations for the great 1906 California earthquake. *Bulletin of the Seismological Society of America*, 95(3), 861–877. https://doi.org/10.1785/0120040141

López Comino, J. A., Cesca, S., Heimann, S., Grigoli, F., Milkereit, K., Dahm, T., & Zang, A. (2017). Characterization of hydraulic fractures growth during the Aspo Hard Rock Laboratory experiments (Sweden). *Journal of Rock Mechanics and Rock Engineering*, 50(11), 2985–3001. https://doi.org/10.1007/s00603-017-1285-0

Manthei, G., Eisenblätter, J., & Kamlot, P. (2003). Stress measurements in salt mines using a special borehole tool. In *Proc Int. Symp. on Geotechnical Measurements and Modelling* (pp. 355–360). AA Balkema, Rotterdam: Karlsruhe, Germany.

Martínez-Garzón, P., Bohnhoff, M., Kwiatek, G., & Dresen, G. (2013). Stress tensor changes related to fluid injection at The Geysers geothermal field, California. *Geophysical Research Letters*, 40, 2596–2601. https://doi.org/10.1002/grl.50438

Martínez-Garzón, P., Kwiatek, G., Bohnhoff, M., & Dresen, G. (2016). Impact of fluid injection on fracture reactivation at The Geysers geothermal field. *Journal of Geophysical Research: Solid Earth*, 121, 7432–7449. https://doi.org/10.1002/2016JB013137

Martínez-Garzón, P., Kwiatek, G., Bohnhoff, M., & Dresen, G. (2017). Volumetric components in the earthquake source related to fluid injection and stress state. *Geophysical Research Letters*, 44, 800–809. https://doi.org/10.1002/2016GL071963

Maxwell, S. C. (2011). What does microseismic tell us about hydraulic fracture deformation, CSEG Rec. - Focus Artic., 36(8).

Maxwell, S. C. (2013). Unintentional seismicity induced by hydraulic fracturing, *CSEG Rec. - Focus Artic.*, *38*(8).

Maxwell, S. C., Shemeta, J. E., Campbell, E., & Quirk, D. J. (2008). Microseismic deformation rate monitoring, in *SPE-116596-MS*, Society of Petroleum Engineers, SPE.

Maxwell, S. C., Zhang, F., & Damjanac, B. (2015). Geomechanical modeling of induced seismicity resulting from hydraulic fracturing. *The Leading Edge*, *34*(6), 678–683. https://doi.org/10.1190/tle34060678.1

McGarr, A. (2014). Maximum magnitude earthquakes induced by fluid injection. *Journal of Geophysical Research: Solid Earth*, *119*, 1008–1019. https://doi.org/10.1002/2013JB010597

Meier, P. M., Rodrigues, A. A., & Bethmann, F. (2015). Lessons learned from Basel: New EGS projects in Switzerland using multistage stimulation and a probabilistic traffic light system for the reduction of seismic risk, in *Proceedings of World Geothermal Congress 2015, Melbourne,* 19-25 *April* 2015, Melbourne.

Metropolis, N., Rosenbluth, A., Rosenbluth, M., Teller, A., & Teller, E. (1953). Equation of state calculations by fast computing machines. *The Journal of Chemical Physics*, *21*(6), 1087–1092. https://doi.org/10.1063/1.1699114

Milkereit, C., Dahm, T., Cesca, S., Lopez, J., Nooshiri, N., & Zang, A. (2017). Long-period tilt-induced accelerations associated with hydraulic fracturing. In *EGU General Assembly Conference Abstracts* (Vol. 19, p. 14472).

Nakatani, M., Yabe, Y., Philipp, J., Morema, G., Stanchits, G., & Dresen, G. (2008). Acoustic emission measurements in a deep gold mine in South Africa—Project overview and some typical waveforms. *Seismological Research Letters*, *79*(2), 311.

Niitsuma, H., Nagano, K., & Hisamatsu, K. (1993). Analysis of acoustic emission from hydraulically induced tensile fracture of rock. *Journal of Acoustic Emission*, *11*, S1–S18.

Norris, J. Q., Turcotte, D. L., Moores, E. M., Brodsky, E. E., & Rundle, J. B. (2016). Fracking in tight shales: What is it, what does it accomplish, and what are its consequences? *Annual Review of Earth and Planetary Sciences*, *44*(1), 321–351. https://doi.org/10.1146/annurev-earth-060115-012537

Plenkers, K., Kwiatek, G., Nakatani, M., Dresen, G., & J. Group (2010). Observation of seismic events with frequencies $f > 25$ kHz at Mponeng deep gold mine, South Africa. *Seismological Research Letters*, *81*(3), 467–479. https://doi.org/10.1785/gssrl.81.3.467

Raleigh, C. B., Healy, J. H., & Bredehoeft, J. D. (1976). An experiment in earthquake control at Rangely, Colorado. *Science*, *191*(4233), 1230–1237. https://doi.org/10.1126/science.191.4233.1230

Ripperger, J., Ampuero, J.-P., Mai, P. M., & Giardini, D. (2007). Earthquake source characteristics from dynamic rupture with constrained stochastic fault stress. *Journal of Geophysical Research*, *112*, B04311. https://doi.org/10.1029/2006JB004515

Rutledge, J., Yu, X., & Leaney, S. (2015). Microseismic shearing driven by hydraulic-fracture opening: An interpretation of source-mechanism trends. *The Leading Edge*, *34*(8), 926–934. https://doi.org/10.1190/tle34080926.1

Schoenball, M., Dorbath, L., Gaucher, E., Wellmann, J. F., & Kohl, T. (2014). Change of stress regime during geothermal reservoir stimulation. *Geophysical Research Letters*, *41*, 1163–1170. https://doi.org/10.1002/2013GL058514

Shapiro, S. A., Rothert, E., Rath, V., & Rindschwentner, J. (2002). Characterization of fluid transport properties of reservoirs using induced microseismicity. *Geophysics*, *67*(1), 212–220. https://doi.org/10.1190/1.1451597

Stanchits, S., Mayr, S., Shapiro, S., & Dresen, G. (2011). Fracturing of porous rock induced by fluid injection. *Thermo-Hydro-Chemo-Mechanical Couplings in Rock Physics and Rock Mechanics*, *503*(1–2), 129–145. https://doi.org/10.1016/j.tecto.2010.09.022

Staněk, F., & Eisner, L. (2017). Seismicity induced by hydraulic fracturing in shales: A bedding plane slip model. *Journal of Geophysical Research: Solid Earth*, *122*, 7912–7926. https://doi.org/10.1002/2017JB014213

Staub, I., Andersson, J. C., & Magnor, B. (2004). Äspö Pillar Stability Experiment, Geology and mechanical properties of the rock in TASQ, SKB R-04-01, Svensk Kärnbränslehantering AB.

Terakawa, T. (2014). Evolution of pore fluid pressures in a stimulated geothermal reservoir inferred from earthquake focal mechanisms. *Geophysical Research Letters*, *41*, 7468–7476. https://doi.org/10.1002/2014GL061908

Terakawa, T., Miller, S. A., & Deichmann, N. (2012). High fluid pressure and triggered earthquakes in the enhanced geothermal system in Basel, Switzerland. *Journal of Geophysical Research*, *117*, B07305. https://doi.org/10.1029/2011JB008980

Vavryčuk, V. (2014). Iterative joint inversion for stress and fault orientations from focal mechanisms. *Geophysical Journal International*, *199*(1), 69–77. https://doi.org/10.1093/gji/ggu224

Wadati, K., & Oki, S. (1933). On the travel time of earthquake waves. (Part II). *Journal of the Meteorological Society of Japan. Ser. II*, *11*(1), 14–28. https://doi.org/10.2151/jmsj1923.11.1_14

Waldhauser, F., & Ellsworth, W. L. (2000). A double-difference earthquake location algorithm: Method and application to the northern Hayward Fault, California. *Bulletin of the Seismological Society of America*, *90*(6), 1353–1368. https://doi.org/10.1785/0120000006

Walsh, F. R., & Zoback, M. D. (2016). Probabilistic assessment of potential fault slip related to injection-induced earthquakes: Application to north-central Oklahoma, USA. *Geology*, *44*(12), 991–994. https://doi.org/10.1130/G38275.1

Warpinski, N. (2014). Microseismic monitoring—The key is integration. *The Leading Edge*, *33*(10), 1098–1106. https://doi.org/10.1190/tle33101098.1

Warpinski, N. R. (2013). Understanding hydraulic fracture growth, Effectiveness, and Safety Through Microseismic Monitoring, in *Effective and Sustainable Hydraulic Fracturing*. (Chapter 6, pp. 123–138). Rijeka, Croatia: IntechOpen. https://doi.org/10.5772/55974

Warpinski, N. R., Du, J., & Zimmer, U. (2012). Measurements of hydraulic-fracture-induced seismicity in gas shales, in *SPE-151597-MS*, Society of Petroleum Engineers, SPE.

Warpinski, N. R., Wright, T. B., Uhl, J. E., Engler, B. P., Drozda, P. M., Peterson, R. E., & Branagan, P. T. (1999). Microseismic monitoring of the B-sand hydraulic-fracture experiment at the DOE/GRI multi-site project, *SPE-57593-PA*. https://doi.org/10.2118/57593-PA

Wiemer, S., & Wyss, M. (2000). Minimum magnitude of completeness in earthquake catalogs: Examples from Alaska, the Western United States & Japan. *Bulletin of the Seismological Society of America*, *90*, 859–869. https://doi.org/10.1785/0119990114

Yeck, W. L., Hayes, G. P., McNamara, D. E., Rubinstein, J. L., Barnhart, W. D., Earle, P. S., & Benz, H. M. (2017). Oklahoma experiences largest earthquake during ongoing regional wastewater injection hazard mitigation efforts. *Geophysical Research Letters*, *44*, 711–717. https://doi.org/10.1002/2016GL071685

Yoon, J. S., Zimmermann, G., Zang, A., & Stephansson, O. (2015). Discrete element modeling of fluid injection–induced seismicity and activation of nearby fault. *Canadian Geotechnical Journal*, *52*(10), 1457–1465. https://doi.org/10.1139/cgj-2014-0435

Zang, A., Oye, V., Jousset, P., Deichmann, N., Gritto, R., McGarr, A., et al. (2014). Analysis of induced seismicity in geothermal reservoirs—An overview. *Analysis of Induced Seismicity in Geothermal Operations*, *52*(0), 6–21. https://doi.org/10.1016/j.geothermics.2014.06.005

Zang, A., Stephansson, O., Stenberg, L., Plenkers, K., Specht, S., Milkereit, C., et al. (2017). Hydraulic fracture monitoring in hard rock at 410 m depth with an advanced fluid-injection protocol and extensive sensor array. *Geophysical Journal International*, *208*(2), 790–813. https://doi.org/10.1093/gji/ggw430

Zang, A., Stephansson, O., & Zimmermann, G. (2017). Keynote: Fatigue hydraulic fracturing. *ISRM European Rock Mechanics Symposium - EUROCK, 191*(191), 1126–1134. https://doi.org/10.1016/j.proeng.2017.05.287

Zang, A., Yoon, J. S., Stephansson, O., & Heidbach, O. (2013). Fatigue hydraulic fracturing by cyclic reservoir treatment enhances permeability and reduces induced seismicity. *Geophysical Journal International, 195*(2), 1282–1287. https://doi.org/10.1093/gji/ggt301

Zhao, P., Kühn, D., Oye, V., & Cesca, S. (2014). Evidence for tensile faulting deduced from full waveform moment tensor inversion during the stimulation of the Basel enhanced geothermal system. *Anal. Induc. Seism. Geotherm. Oper., 52*(0), 74–83. https://doi.org/10.1016/j.geothermics.2014.01.003

Zhou, H. (1994). Rapid three-dimensional hypocentral determination using a master station method. *Journal of Geophysical Research, 99*(B8), 15,439–15,455. https://doi.org/10.1029/94JB00934

Ziegler, M., Heidbach, O., Zang, A., Martínez-Garzón, P., & Bohnhoff, M. (2017). Estimation of the differential stress from the stress rotation angle in low permeable rock. *Geophysical Research Letters, 44*, 6761–6770. https://doi.org/10.1002/2017GL073598